

High-Accuracy Near-infrared Imaging Polarimetry with NICMOS

D. BATCHELDOR

Center for Imaging Science, Rochester Institute of Technology Rochester, NY 14623; dan@astro.rit.edu

G. SCHNEIDER

Steward Observatory, The University of Arizona Tucson, AZ 85721; gschneider@as.arizona.edu

D. C. HINES

Space Science Institute Boulder, CO 80301; dhines@as.arizona.edu

G. D. SCHMIDT

Steward Observatory, The University of Arizona Tucson, AZ 85721; schmidt@chinadoll.as.arizona.edu

D. J. AXON

Department of Physics, Rochester Institute of Technology Rochester, NY 14623; djasps@rit.edu

A. ROBINSON

Department of Physics, Rochester Institute of Technology Rochester, NY 14623; axrps@rit.edu

W. SPARKS

Space Telescope Science Institute Baltimore, MD 21218; sparks@stsci.edu

C. TADHUNTER

Department of Physics & Astronomy, University of Sheffield, Sheffield S3 7RH, United Kingdom; C.Tadhunter@sheffield.ac.uk

Received 2008 November 3; accepted 2008 December 27; published 2009 February 04

ABSTRACT. The findings of a nine-orbit calibration plan carried out during *HST* Cycle 15, to fully determine the NICMOS camera 2 ($2.0\ \mu\text{m}$) polarization calibration to high accuracy, are reported. Recently Ueta et al. and Batcheldor et al. have suggested that NICMOS possesses a residual instrumental polarization at a level of 1.2%–1.5%. This would completely inhibit the data reduction in a number of GO programs, and hamper the ability of the instrument to perform high-accuracy polarimetry. We obtained polarimetric calibration observations of three polarimetric standards at three spacecraft roll angles separated by $\sim 60^\circ$. Combined with archival data, these observations were used to characterize the residual instrumental polarization in order for NICMOS to reach its full potential of accurate imaging polarimetry at $p \approx 1\%$. Using these data, we place an 0.6% upper limit on the instrumental polarization and calculate values of the parallel transmission coefficients that reproduce the ground-based results for the polarimetric standards. The uncertainties associated with the parallel transmission coefficients, a result of the photometric repeatability of the observations, are seen to dominate the accuracy of p and θ . However, the updated coefficients do allow imaging polarimetry of targets with $p \approx 1.0\%$ at an accuracy of $\pm 0.6\%$ and $\pm 15^\circ$. This work enables a new caliber of science with *HST*.

1. INTRODUCTION

Polarimetry is a powerful observational tool that augments and complements the capabilities of imaging, photometry and spectroscopy. While the latter allow the determination of spatial distributions, chemical composition, and dynamics, polarimetry lets us observe the nature of magnetic fields, object orientation, scattering, and the properties of interstellar particles in general. It also allows us to probe the nature of emission

mechanisms (e.g., synchrotron or thermal), and to investigate the geometry of unresolved sources.

The value of polarimetry to elucidate the physical nature of light-scattering particles and their environments in astrophysical systems has been repeatedly demonstrated in, for example, active galactic nuclei (Antonucci & Miller 1985; Capetti et al. 1995), galactic and extragalactic magnetic fields (Wielebinski 1995), radio galaxies (Feretti et al. 1998; Vernet et al. 2001),

and circumstellar disks (Kuhn et al. 2001). However, because of “beam depolarization,” results derived from polarimetric imaging observations may be biased when obtained at low spatial resolution. For example, compact (but spatially resolved) objects that exhibit circular symmetry or biconical structures, like active galactic nuclei (AGNs) and stars surrounded by orbiting circumstellar dust, contain polarized elements that partially reduce, if not fully cancel, each other when spatially averaged. If the object is unresolved, then the polarization vectors sum to *zero*; in any case, beam depolarization will always underestimate the intrinsic polarization.

The Near-Infrared Camera and Multi-Object Spectrometer (NICMOS) is the *only* near-infrared (NIR) instrument capable of the high-resolution, high-fidelity polarimetry needed to examine the scattering geometry and materials, in detail, for many types of astronomical objects. To date, there have been a multitude of studies carried out using NICMOS direct-imaging polarimetry (e.g., Capetti et al. 2000; Tadhunter et al. 2000; Silber et al. 2000; Schmidt et al. 2002; Simpson et al. 2002; Su et al. 2003; Meakin et al. 2005; Simpson et al. 2006) and there are now more ambitious programs to measure the characteristics of AGNs and regions within circumstellar protoplanetary debris disks, which typically exhibit polarizations of less than 5% (Smith et al. 2004; Schneider et al. 2005). However, there have been recent reports of a systematic residual instrumental polarization of $\sim 1.5\%$ in some objects (Ueta et al. 2005), which, although acceptable for highly polarized targets, seriously compromises studies of low polarization objects. A comprehensive study of this residual polarization has been carried out by Batcheldor et al. (2006 [hereafter B06]). Using all of the available standard polarization data in the archives, B06 indeed find a residual excess polarization of $\approx 1.2\%$ in the NIC2 camera. The extent of this excess remains unknown for NIC1.

Unfortunately, prior to the new calibration reported in this paper, since the advent of the NICMOS cooling system (NCS; Schneider 2004), installed during SM3B in 2002, observations of only one polarized and one unpolarized standard have been obtained, and each at only two celestial orientation angles. Hence, it has been impossible, with those limiting data, to entirely characterize the NICMOS residual polarization. Polarization measurements at three well-separated roll angles are required to remove the dependence of the measured Stokes parameters on the relative transmission of each of the filters.

This paper reports the findings of a nine-orbit *Hubble Space Telescope* (*HST*) calibration plan (Cycle 15), to fully investigate the residual polarization in NICMOS. NICMOS carries two cameras with polarimetry optics designated NIC1 and NIC2 (a third camera for wide-field and grism imaging has no polarimetry capability). NIC1 provides an $11'' \times 11''$ field of view (FOV) with an image scale of $43.1 \text{ mas pixel}^{-1}$ and $1.045 \mu\text{m}$ broadband ($0.475 \mu\text{m}$ FWHM; $R = \Delta\lambda/\lambda = 45\%$) polarizing filters. NIC2 (the primary focus of this paper) provides a $19.3'' \times 19.2''$ FOV with 75.8 mas pixels and a

medium-bandwidth polarimetric passband of $1.994 \mu\text{m}$ ($0.202 \mu\text{m}$ FWHM; $R = 10\%$). Both optical channels critically sample the respective point-spread functions (PSFs) in their polarimetric passband. For additional details of the NICMOS instrument, see Thompson et al. (1998) and the NICMOS Instrument Handbook (Barker et al. 2007). The two cameras have noncommon path optics from the instrument’s field divider mirror assembly to their respective reimaged focal-plane detectors. As polarimetric imaging in the two cameras is (uniquely) carried out at different wavelengths, there is no reason to expect the same level of residual instrumental polarization in each camera. With this in mind we carried out observing plans to push the NIC2 calibration to its instrumental limit, given the intrinsically superior polarimetric performance of the NIC2 camera over NIC1 (Hines et al. 2000). Due to the nature of NIC1, we confine the results from this camera to the Appendix. In § 2 we describe the observing strategy employed, and in § 3 we explain the data reduction procedures. A detailed examination of the photometry is completed in § 3.1. The results and methods are presented in § 4 before being discussed in § 5 and concluded in § 6. A recommended observing plan for NICMOS imaging polarimetry with NIC2 is included in § 5.1.

2. OBSERVATIONS

The NIC2 observations were designed to be totally comprehensive in the sense that they were made to address not only the NICMOS residual polarization but also several other key issues including possible dependence with detector quadrants, source color dependence, the interpixel response functions (IPRFs), and latent image persistence. The details of the observations are summarized in Table 1.

Image persistence (or latent image decay) can contribute significantly to photometric errors in sequential exposures of bright targets on the same pixel locations on the focal-plane array. The same is also true for cosmic ray hits; therefore all observations were scheduled in orbits that were not impacted by the South Atlantic Anomaly. As NICMOS polarimetric analysis derives intensity differences from measures obtained in each of its three camera-specific polarizing filters, systematic differences due to image persistence or other instrumental causes, should be circumvented or minimized to the greatest degree possible. Persistence can be overcome with an effective image dithering strategy. The diffraction spikes arising from the *HST* secondary mirror support in the *HST* + NICMOS PSF can contain a large number of photons, so a precise dithering pattern must be carefully chosen. In our calibration observations, custom dither patterns were created for each camera.

In the absence of superdark calibration frames, which replicate to very high fidelity the behavior of the NICMOS detectors as specifically clocked for any given science observation, both quadrant-dependent and global-bias offsets often arise in basic (pipeline) calibrations (both are frequently seen when calibration database, calibration library, or synthetic dark frames are

TABLE 1
DETAILS OF OBSERVATIONS

Target	DATE-OBS	ORIENTAT	Camera	<i>T</i> (s)
[VR84] c	2007 May 03	182.2°	NIC1	3.6
	2007 Aug 03	299.3°		
	2006 Dec 15	59.2°		
	2007 May 03	181.4°	NIC2	
	2007 Aug 03	298.6°		
	2006 Dec 15	58.4°		
VSS VIII-13	2006 Aug 04	180.3°	NIC1	1.6
	2006 Jun 25	114.3°		
	2007 Apr 11	54.3°		
	2006 Aug 04	179.6°	NIC2	
	2006 Jun 25	113.6°		
	2007 Apr 11	53.6°		
HD 331891	2006 Aug 27	273.8°	NIC1	1.6
	2006 Jul 01	338.4°		
	2007 Apr 15	38.3°		
	2006 Aug 27	273.1°	NIC2	
	2006 Jul 01	337.6°		
	2007 Apr 15	37.5°		

NOTE.—Each observation was performed at three different roll angles and for the POL0, POL120, and POL240 polarizers. In total, NIC2 was dithered around 36 pointings per orbit, with 12 pointings per polarizer. The DATE-OBS parameter gives the observation date in YYYY-MM-DD format. “ORIENTAT” refers to the celestial position angle of the image +*y* axis (degrees east of north). *T* gives the exposure times in seconds.

employed). However, during this calibration we acquired contemporaneous dark frames to mitigate the possibility of residual systematics in the multiaccum-derived count rate images. These darks were matched to the detector clocking modes used for our targeted observations and executed during the occulted period of each orbit. Nonetheless, to assess the possible impact of “pedestal-like” effects of other instrumental origins, the same observing sequence was repeated with the target repositioned in each of the four detector quadrants. Flat-field artifacts can be enhanced (rather than reduced) in amplification with improperly biased (subtracted) dark reference frames.

The observations in each quadrant were dithered in order to mitigate the effects of the IPRFs and to sample around defective pixels. The IPRFs can alter the count rates from a target simply through different alignments (centerings) with respects to the pixel center at each pointing. The pointing offsets cover a phase spacing of $-1/3$, 0 , and $+1/3$ pixels in order to best tile the IPRFs for the dither pattern employed. In addition, the dither step sizes are greater than the radius of the third Airy PSF minima ($0.58''$, 7.6 pixels). The orientation of the dither pattern was rotated, with respect to the detector rows and columns, by 22.5° to remove the possibility of overlapping persistence from

the PSF diffraction spikes of previous pointings. Figure 1 shows an overlay of the NIC2 pointings from within one orbit.

These observations were repeated for each of the three chosen polarimetric standard stars and at three separate spacecraft roll angles, i.e., three celestial orientation angles of the camera aperture on the sky. This enables a unique determination of any residual instrumental polarization, above the detection floor, relative to the equatorial reference frame. More crucially, this multi-orientation technique means that the polarimetric analysis derived from the three polarizers at each of the field orientations can be completely and uniquely decoupled and checked for consistency. This method also removes the dependence of the measured Stokes parameters on the relative transmission of each of the polarizing filters and, at the same time, any dependence of the instrumental polarization on the detector’s sensitivity to polarized light.

Light scattering within the instrument could, at least in part, be largely responsible for the observed residual instrumental polarization, but light scattering is wavelength dependent, so standard stars with intrinsically different spectral energy distributions were chosen. The details of the three polarimetric standards picked for this calibration are summarized in Table 2. As *HST* was operating in two gyro during *HST* Cycle 15 (the epoch

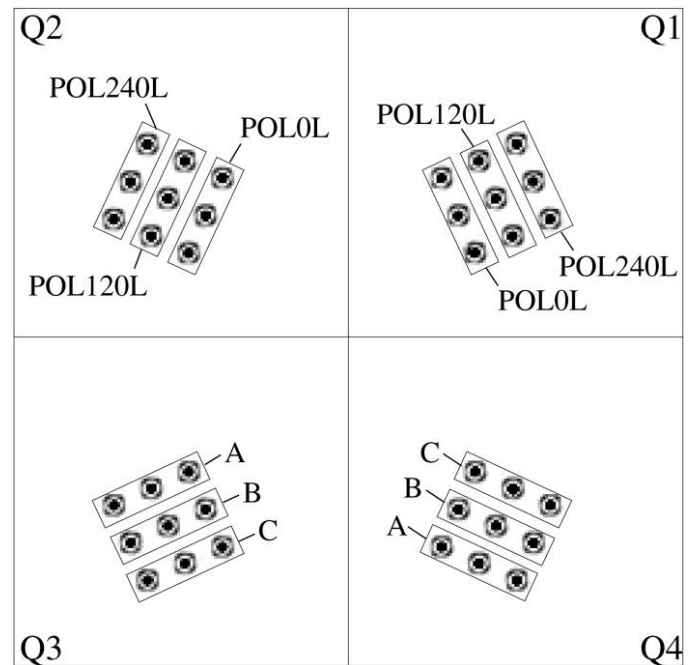


FIG. 1.—Example from one orbit of the NIC2 pointings used to determine the effects of the IPRFs, quadrant dependence and persistence. POL0L, POL120L, and POL240L observations are in the inner, middle, and outer diamonds of points respectively. The “A”, “B,” and “C” positions are used to index the dithered pointings of each polarizer. The POL0L, POL120L, POL240 and A, B, C markings, which are both applicable to each quadrant, are used to define the pointing naming convention. For example, the lowest pointing on the left of the array would be POL240L-Q3-C.

TABLE 2
DETAILS OF POLARIMETRIC STANDARDS

TARGET	TYPE	m_v	m_j	m_k	(p, θ)				
					p IS IN PERCENT; θ IS IN DEGREES				
					0.55 μm	1.05 μm	1.21 μm	2.00 μm	2.04 μm
[VR84] c (WKK F7)	B5V	10.3	9.34	9.13	5.98, 118	4.04, 118 ^a	3.19, 118	1.25, 126 ^a	1.19, 126
VSS VIII-13	K1III	12.7	9.65	8.68	2.25, 102	2.49, 99 ^a	2.21, 96	0.91, 102 ^a	0.86, 102
HD 331891	A4III	9.3	8.80	8.72	0.04, n/a

NOTE.—Basic data for the observed polarimetric standards. Two polarized and one unpolarized star (HD 331891).

^aValues that have been corrected using the Serkowski curve. There is no method to precisely determine θ at 1.05 and 2.00 μm , so the average values between 0.55 and 1.21 μm , and the values at 2.04 μm are used respectively. More details for each target are given in the text.

of all the calibration observations—see Table 1), the dominant factor in the selection of this sample was the availability of the three separate roll angles required to allow polarization measurements to be derived from the single polarizers.

2.1. Calibration Targets

All targets were sufficiently bright so that the PSF central pixel approached the full-well depth near the end of the nondestructive sequence of readouts in each multiaccum exposure. This maximized the photon signal-to-noise ratio (S/N) with the greatest observing efficiency. In addition, as the exposure times were short (Table 1), the target brightnesses ensured each could be observed multiple times within its dither pattern during one orbit.

[VR84] c (WKK F 7, Cha DC F7) was chosen as it has a significant percentage polarization in both the J and K bands, and as it had been observed in the previous polarimetric calibrations of NICMOS; it serves as a control. Whittet et al. (1992) give a K-band polarization of $1.19\% \pm 0.01\%$ at $126^\circ \pm 4^\circ$.

The second polarimetric standard VSS VIII-13 (R CrA DC No. 13) was also chosen for its percentage polarization. However, it is also found in a different association from [VR84] c, making it more suitable as a calibration target. Within any given association, measured stellar polarization angles tend to be similar. This implies a polarization process internal to the association. Whittet et al. (1992) give a K-band polarization of $0.9\% \pm 0.2\%$ at $102^\circ \pm 5^\circ$.

The final standard, HD 331891, was chosen because it was found to have an insignificant amount of polarization at 0.55 μm ($0.04\% \pm 0.02\%$) by Turnshek et al. (1990). It too was observed in previous calibration projects. There are no data of this target at 2.00 μm (previous to this study), therefore we have to cautiously assume that it remains unpolarized at this wavelength.

Comparison of NICMOS and ground-based polarization measurements must be band-transformed through the known wavelength dependence of interstellar polarization (Serkowski et al. 1975). The ground-based results are derived from observations at 1.21 and 2.04 μm and are corrected to 1.05 and 2.0 μm using the “Serkowski curve” (Serkowski 1973; Wilking

et al. 1982). These values are listed in Table 2 and are used in this study as the ground-based comparison values. We also propagate the uncertainties of each ground-based measurement in our analysis.

3. DATA REDUCTION

The “raw” multiaccum exposures were used to create individual instrumentally calibrated count rate images for each target pointing. Calibration steps included “DC bias” offset corrections with respect to the contemporaneously obtained reference dark frames, “superzero” signal accumulation compensation, read-by-read dark subtraction, read-by-read linearity correction, cosmic-ray identification and reparation, saturation threshold determination, flat-field correction, weighted-least-squares count rate solution, bad pixel reparation by 2D interpolation of good neighbors, and the removal of the telescope (+ sky) thermal background. Before continuing, each image was checked for possible latent image persistence resulting from the previous image. No image latency was found in any of the individual multiaccum exposures.

3.1. Photometric Analysis

It is essential to individually evaluate the fidelity of each pointed observation. An ideal imaging detector would produce precisely the same photometry with the target located at any arbitrary position on the grid of detector pixels and would make polarimetric analysis fairly straightforward. Polarimetry, by its very nature, is highly sensitive to small variations in the photometry, and in any instrumental system there are many factors that can compromise the data. Sources of small variations in the photometry that do not directly result from the intrinsic polarization of the target and that have not already been accounted for must be identified and removed.

Aperture photometry was performed at each pointing using the `digiphot` package within IRAF.² Radially incremented

²IRAF is distributed by the National Optical Astronomy Observatories, which are operated by the Association of Universities for Research in Astronomy, Inc., under cooperative agreement with the National Science Foundation.

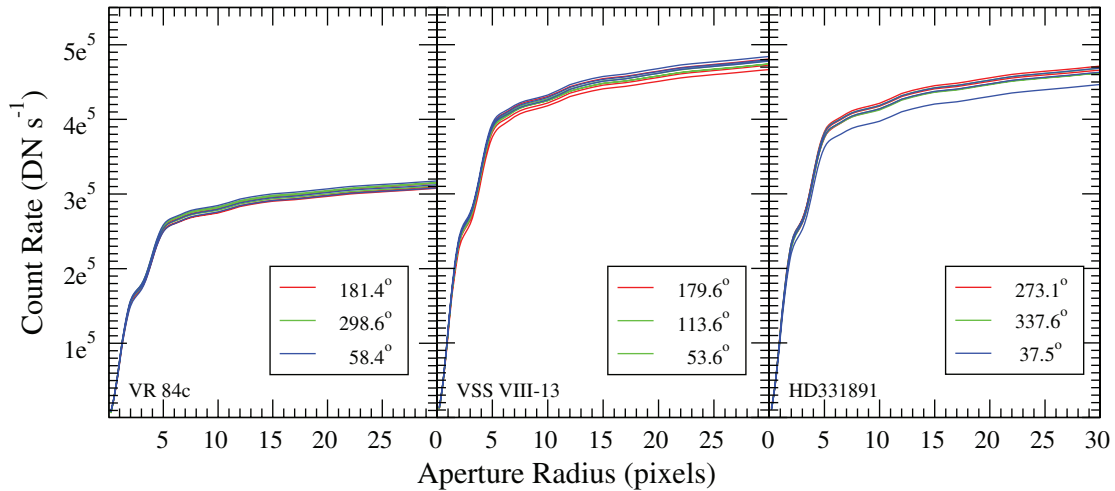


FIG. 2.—For each target, the encircled count rate summed over all dither positions, for each polarizer and target field celestial orientation, is shown. The inflexions due to the PSF are clearly visible, as are some deviant profiles (e.g., HD 331891 at 37.5°). In all cases, 95% of the total flux is with a radius of 20 pixels, 99.9% is at 50 pixels.

circular apertures were placed on the target. The (subpixel) centers were determined using the intensity weighted means of the profiles in the x and y directions. The encircled count rates through the radially increasing apertures were then extracted.

The summed extracted NIC2 radial profiles from the same polarizer at the separate position angles are presented in Figure 2. From this a number of effects are observed. First, the Airy pattern component of the PSF is seen in the radial profile inflexions. Second, there are some profiles that are inconsistent with the majority due to nonrepeatability effects in the photometry beyond those mitigated by our observing strategy and image calibration. Finally, there is a noticeable spread in the count rates; more than one expects from polarization alone.

Each individual radial profile was compared to the average profile from the 12 individual dithers. The offset of each individual radial profile from the average profile was determined as a function of radius. Any encircled radial profile that showed more than a 2σ deviation from the average profile was flagged and inspected. Figure 3 spatially plots the positions of the flagged profiles using the filled squares. In all, 10% of the profiles show deviations of $>2\sigma$ from the original average profile.

About 40% of the deviant profiles (4% of all the pointings) are the result of the individual target pointings placing the center of the stellar PSF on uncorrectable bad pixels (excessive grot, i.e., pixels with reduced throughput due to particulate contamination on the detector³). In this case it is impossible to recover the lost flux, and these pointings are discarded from further study. These profiles are typically clustered around the Q1-A positions.

³ For more information, see http://www.stsci.edu/hst/nicmos/documents/isrs/isr_99_008.pdf.

As expected, in $\sim 20\%$ of the deviant cases the pointings have fallen close to the coronagraphic hole. The profiles are clustered around the Q2-A positions. With time, the precise position of the hole wanders by ~ 1 pixel. However, its position (x, y) is

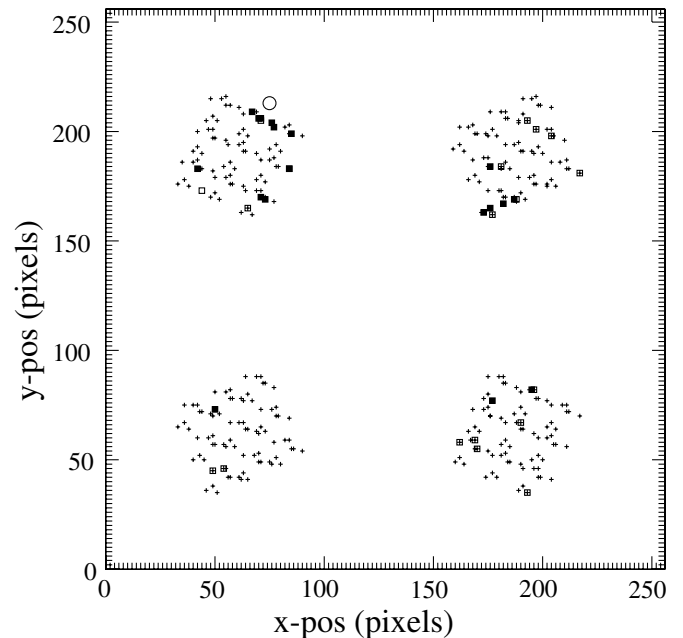


FIG. 3.—Identifying NIC2 deviant profiles. The open circle ($r = 0.3''$, 4 pixels) marks the position and geometrical size of the coronagraphic hole projected onto the detector. However, the afocal imprint of the hole can affect $2.0\ \mu\text{m}$ circum-hole photometry (at our 2σ rejection level) to a distance of $\sim 0.6''$. Plus signs show the positions of all the pointings from all nine orbits. The filled squares are profiles that show $>2\sigma$ deviations at all radii. The open squares are profiles that only show $>2\sigma$ deviations within a radius of two pixels.

typically 73.5, 213.5 with a soft edge that can extend to a radius of 7 pixels. Data that were affected by the presence of the coronagraph were excluded.

The remaining flagged profiles show $>2\sigma$ deviations at radii of ≤ 2 pixels. As the NIC2 polarizers have an effective wavelength of $1.995\ \mu\text{m}$, and the effective primary aperture is 2.281 m (as defined by the NIC2 pupil mask), the theoretical PSF core diameter is $0.22''$ or 2.91 pixels (PSF FWHM = $0.185''$, 2.44 pixels); NIC2 critically samples the PSF. As these profiles are only deviant within the diffraction limit of the instrument, and are within 2σ of the average profiles at radii >2 pixels; i.e., the effects are negated by increasing the aperture size, and they are not excluded from further study.

The processes of flagging and inspecting deviant profiles were repeated until all profiles fell within 2σ of the average. At each iteration, excluded profiles were removed from the original average. In the worst case, only three profiles (from 12) were rejected.

3.2. Achievable Accuracies

In polarimetric analyses, the accuracies that are achievable are determined by the S/N of the data. Therefore, in order to estimate the effects of background noise, the 12 NIC2 images in each polarizer were combined, after precise astrometric registration, into a single median image. In all cases, images were first aligned using the spacecraft pointing information provided in the `.fits` headers of the raw files. This coregistered the images with a relative precision of a few tenths of a pixel. Subsequent “fine” alignments of the intersit images were performed using an apodized bicubic resampling of the stellar PSF cores onto a $32\times$ (in both x and y) larger grid. The resampled individual images were then shifted to a common fiducial position by the difference in centroids found iteratively with least-squares 2D Gaussian profile fitting. This process was repeated 3 times and converged all reregistered image centroids to a few thousandths of a pixel.

The pixel-to-pixel noise in the combined polarimetric total intensity images (Stokes I) was found by measuring (in each image) the standard deviation in the “background” region. The region was close enough to the target that all 12 backgrounds from the individual images contributed to the combined image, but sufficiently far out so that no flux from the target itself contributed to the background. A 151×151 -pixel subarray region, centered on the target, was used. Flux from the diffraction spikes was masked. To find the region beyond which the target did not contribute to the background, square masks, increasing in size iteratively, were placed in the photometric aperture. As the mask was incremented (in 2 pixel lengths and widths) from 90 to 100 pixels, earlier (smaller mask size) standard deviations ceased to decrease, and both the median and mean were consistent with zero. Therefore, a square mask of 100×100 pixels, plus a diffraction spike mask, were used and noise statistics were computed on 10,660 pixels. In all

cases, the peak pixels (with instrument intensities of several thousand counts per second) typically have a 1σ noise of 0.1 to 0.2 counts per second; the per-pixel data is photon noise dominated.

As shown by Sparks & Axon (1999 [hereafter SA99]), the S/N averaged across the three polarizers ($\langle S/N \rangle_k$) times the required polarization degree (p) determines the accuracy to which polarimetry can be performed (σ_p) in the photon noise dominated regime. Equation (1), taken from SA99 (their section 7.4), demonstrates the relationship between $\langle S/N \rangle_k$ and σ_p . It does not take into account any instrumental polarization nor any differences in the PSFs between polarizers and assumes that the polarizers are perfect:

$$\log_{10}(\sigma_p/p) = -0.102 - 0.9898 \log_{10}(p\langle S/N \rangle_k). \quad (1)$$

Given p and S/N we can use equation (1) to calculate the theoretical achievable polarimetric accuracies in the absence of non-photon-noise dominated statistics, as illustrated in Figure 4. It can be seen (by looking at the intercepts of the highest dashed horizontal line and the $\pm 0.2\%$ curve) that the observations theoretically allow measurements of $p = 1.0\% \pm 0.2\%$ for [VR84] c.

However, as a single NIC2 pixel spatially undersamples the PSF through the polarizers by 59%, accurate polarimetry cannot be done on a single pixel; the image plane of NIC2 better than

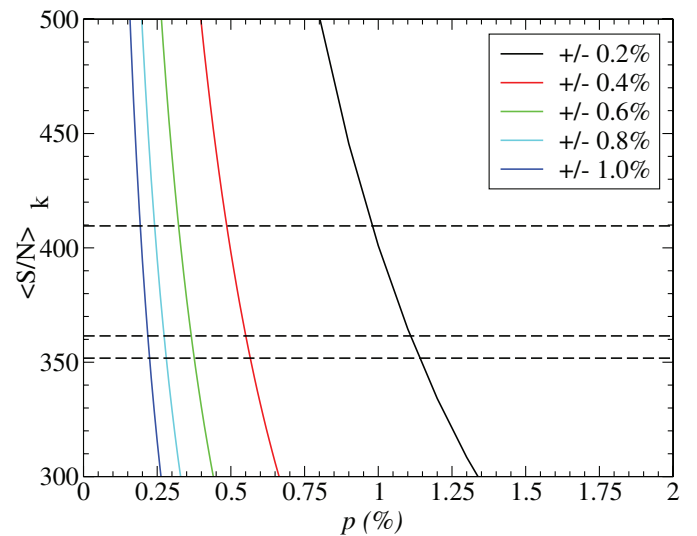


FIG. 4.—Achievable polarimetric accuracies as a function of $\langle S/N \rangle_k$ and intrinsic target polarization (p [%]). The solid colored curves show the increasing uncertainties in p , given by the inset, as p approaches zero for a given $\langle S/N \rangle_k$. The dashed horizontal lines, from top to bottom, are the peak per pixel $\langle S/N \rangle_k$ for [VR84] c, VSS VIII-13, and HD 331891, respectively, averaged across all three polarizers. For example, using the data collected on [VR84] c, we expect to reach accuracies of $p = 1.0\% \pm 0.2\%$ or $0.5\% \pm 0.4\%$ depending on the actual intrinsic polarization of [VR84] c. Polarizations below 0.35% will be consistent with zero as the uncertainties are $\pm 0.6\%$.

critically (Nyquist) samples the FWHM of the PSF. In addition, there are temporal instabilities in the PSF from spacecraft breathing and pupil mask shifts (the three polarizers are used nonsimultaneously). For point-source polarimetry, some spatial binning beyond an instrumental resolution element must be done to improve the accuracy of the polarimetry otherwise affected by the aforementioned instabilities and measurement limitations.

So far we have assumed that the intrinsic pixel calibration uncertainties are largely mitigated through an effective image dithering strategy, as was implemented for NIC2 in this calibration program. However, there remains a clear dispersion in the photometry after dither combination. As expected, this dispersion varies with radius because the diffracted (and scattered) energy extends very far from the central pixel (Fig. 2). In addition, for any fixed radius, the dispersion is also separately affected by target position on the array due to instrumental affects (e.g., imperfect flat fielding and IPRFs that, in detail, differ among detector photodiodes or pixels).

In the point-source case we use the encircled energy curves, from the incrementing radius aperture photometry, to follow the variation in the S/N (and therefore the achievable accuracy). Small temporal variations in the PSF structure of point sources will be largely mitigated by polarimetric analyses done with measurements on sufficiently large target “enclosing” photometric apertures. The optimal size of the photometric measurement aperture will be large enough to minimize the aggregate affects of changes at the pixel level, but not so large as to include data in the noise regime that is not photon dominated. Therefore, the S/N from dithered images is defined as the ratio between the mean of the individual sums of per-pixel measures in each image, and the 1σ (standard deviation) of the sums about that mean (S/N_σ). With this definition we can see the polarimetric accuracy that is possible considering instrumental and telescope systematic effects (e.g., quadrant dependence, IPRF, PSF, telescope breathing).

Figure 5 shows the NIC2 S/N_σ as determined from the 1σ dispersions about the mean in the incremental-radius aperture photometry. The typical S/N_σ that encircles the second Airy maxima is 300. From Figure 4 we see that a polarization measurement of $p = 1.3\% \pm 0.2\%$ is achievable. This is consistent with the pixel-to-pixel $\langle S/N \rangle_k$ accuracy. The S/N_σ that encircles the first Airy maxima gives a possible polarization measure of $p \approx 1.2\% \pm 0.3\%$, inside the first Airy minimum we see $p \approx 1.1\% \pm 0.5\%$ is attainable. Apertures with radii of 7.6 pixels are optimum. Inside this radius S/N_σ is dominated by changes at the pixel level (large variations with radius), outside this radius photon noise begins to dominate (S/N_σ smooths out and turns over). At even larger radii, the target flux will strongly decline so that instrumental noise will dominate.

The achievable accuracies are optimized by using a photometric aperture size of 7.6 pixels ($0.58''$). Moreover, in § 4.1 we will demonstrate that by recalibration of the polarizer transmis-

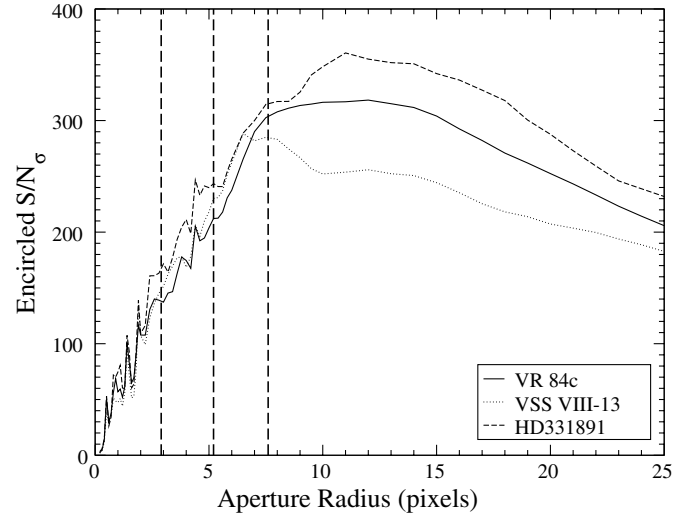


Fig. 5.—Radial variation of S/N_σ in each target. S/N_σ is defined by the values of the average profiles divided by the 1σ dispersions derived from the individual profiles (see text for more details). The three thick vertical dashed lines show the theoretical radii of the first, second, and third Airy minima arising from the diffraction pattern of the centrally obscured primary mirror.

sion coefficients, using our new data set, we can bring the observed values of p and the celestial orientation of polarization (θ) in agreement with the ground-based measurement of the polarized standard stars. However, as demonstrated by Figure 4, in the case of the unpolarized standard, we cannot expect to determine $p = 0\%$ but merely a polarization that is consistent with zero from within the errors.

4. POLARIMETRIC ANALYSIS

The determination of p and θ have been specifically addressed for NIC2 previously (B06; Hines et al. 2000). The coefficients presented in Table 3 (the best available previous determination without the addition of our newly acquired calibration data) are those determined from the Cycle 11 NICMOS polarimetric calibration program (Hines 2002). We briefly revisit the linear technique for the case of three nonideal polarizers below; the case of three “ideal” polarizers (applicable for ACS, but not for NICMOS) is discussed by Capetti et al. (2007).

The instrumental counts per second measured through each polarizing element are used to define an observed intensity vector of the form $a = [I_1, I_2, I_3]$. The Stokes parameters, which also defined a vector $b = [I, Q, U]$, are used to calculate p and θ_f (see eqs. [2] and [3]). The two vectors a and b are simply related to each other by the linear expression $[C]b = a$, where $[C]$ is a matrix describing the characteristics of the k th polarizer, namely the actual orientation (in radians) of the polarizer (ϕ_k), the fraction of the light transmitted in the parallel direction (t_k), and the fraction of light transmitted in the perpendicular direction (the “leak,” l_k). The polarizer efficiency (η_k) is given by $(1 - l_k)/(1 + l_k)$. The linear expression $[C]b = a$ can be solved

TABLE 3
THE PREVIOUS POLARIMETRIC COEFFICIENTS

Polarizer	ϕ_k (deg)	η_k	l_k	t_k
POL0L	8.84	0.7313	0.1552	0.8779
POL120L	131.42	0.6288	0.2279	0.8379
POL240L	248.18	0.8738	0.0673	0.9667

NOTE.—The previous polarization coefficients as derived from the Cycle 11 calibration program.

for (I, Q, U) using LU decomposition. We can then determine p and θ_f using equations (2) and (3):

$$p = 100\% \times \frac{\sqrt{Q^2 + U^2}}{I}; \quad (2)$$

$$\theta_f = \frac{1}{2} \arctan \frac{U}{Q}. \quad (3)$$

In equation (3) a 360° arctangent function is assumed. In addition, the orientation of the frame has to be subtracted from θ_f in order to retrieve the celestial position angle θ . This process has been coded into the IDL routine *polarize.pro*.⁴ This routine takes the three polarized images, calculates (I, Q, U) , and then produces two dimensional maps of p and θ_f . The 1σ dispersions of the count rates around the mean (used to define S/N_σ) have also been used to determine the uncertainties in p and θ . As shown by SA99, the variance and covariance in the (Q, U) plane define the uncertainties in p , $\sigma(p)$ and θ , $\sigma(\theta)$.

In order to demonstrate the limiting accuracy of the previous (Cycle 11) polarimetric calibration, we have applied the Table 3 coefficients to our newly acquired polarimetric standard star observations. Figure 6 demonstrates that only at a few roll angles does this reproduce the ground-based results. In all cases, however, we can see that the results are stable outside of the second Airy maximum.

4.1. The Calibration

It is now that we can begin to exploit the power of observing each standard at multiple spacecraft roll angles; the uncertainties due to the relative filter transmissions can be removed as the same polarizers have been used at three distinct orientations; i.e., each polarizer has separately, and independently, collected all of the necessary polarimetric data. By using polarimetric data gathered in this fashion, the method for calculating p and θ can use invariant transmission coefficients for a given polarizer. In this case the resulting polarization is independent of t_k and is

only affected by ϕ_k (plus the ORIENTAT) and l_k . Due to observation scheduling constraints imposed by *HST*'s 2-Gyro operating mode (in place during Cycle 15) we were unable to obtain our calibration data at ideal differential celestial position angles (see Table 1 for as-executed orientations). Hence, though obtained with three roll angles, we cannot analyze these data as one would through a single perfect polarizer at ideal orientations; the method described in § 4 must still be followed in order to derive the Stokes parameters.

The quantitative results obtained from polarimetric analysis of the apertures enclosing the second Airy maxima, from the three roll orientations using the Cycle 11 derived calibration coefficients (Table 3), are shown in Table 4. These results do not precisely recover the ground-based results listed in Table 2. With the unknowns (t_k) nullified by the three orientations, we assume these residuals to be an instrumental polarization (p_{ins}).

Because $(Q, U)_{\text{ins}}$ is in the instrumental frame, the derived p_{ins} is fixed to the corotating spacecraft frame. Therefore, simply subtracting the observed residual polarizations (found in the unpolarized standard) from the polarized standards is not appropriate; p_{ins} must be determined in Stokes space. For this, as we are calibrating NICMOS against the ground-based results, we determine (I, Q, U) and the associated uncertainties for the standard stars, $(I, Q, U)_{\text{std}}$. However, I is dependent on the nature of each individual observation and the intrinsic polarization of the target, so we must calculate $(Q, U)_{\text{std}}$ as a function of the I observed by NIC2 (I_{nic}). It then follows that we can determine $(Q, U)_{\text{ins}}$ from equation (4), where all vectors have been rotated into the celestial plane:

$$(Q, U)_{\text{ins}} = (Q, U)_{\text{nic}} - (Q, U)_{\text{std}}. \quad (4)$$

We can then use equations (2) and (3) to determine $(p, \theta)_{\text{ins}}$. The results of this are presented in Table 5, which shows the raw Stokes parameters derived from following this method. The instrumental polarization derived from an unweighted average of our observations is $0.6\% \pm 0.1\%$ at $116^\circ \pm 15^\circ$. Attention can now be turned back to the data from the single roll angles. With the instrumental polarization (in Stokes space) determined and subtracted, the only parameter affecting the deviation from the ground-based results is t_k . The values of t_0 and t_{120} that reproduce the ground-based results can then be determined numerically. As in the previous calibrations, t_{240} is held at 0.9667 as it is the long polarizer with the highest efficiency. The other values of t_k can be determined with respects to t_{240} .

As this process was performed by B06 on archival data, we can also include the values of t_k derived by those authors. We limit these additional data to the polarimetric standards observed in the post-NCS era. These data comprise two epochs for [VR84] c (identified as CHA-DC-F7 by B06) and two epochs of data for HD 331891. Table 6 presents the resulting values of t_0 and t_{120} including the derived values of p and θ .

⁴ More details on the Polarizer Data Analysis Software is available online at http://www.stsci.edu/hst/nicmos/tools/polarize_tools.html.

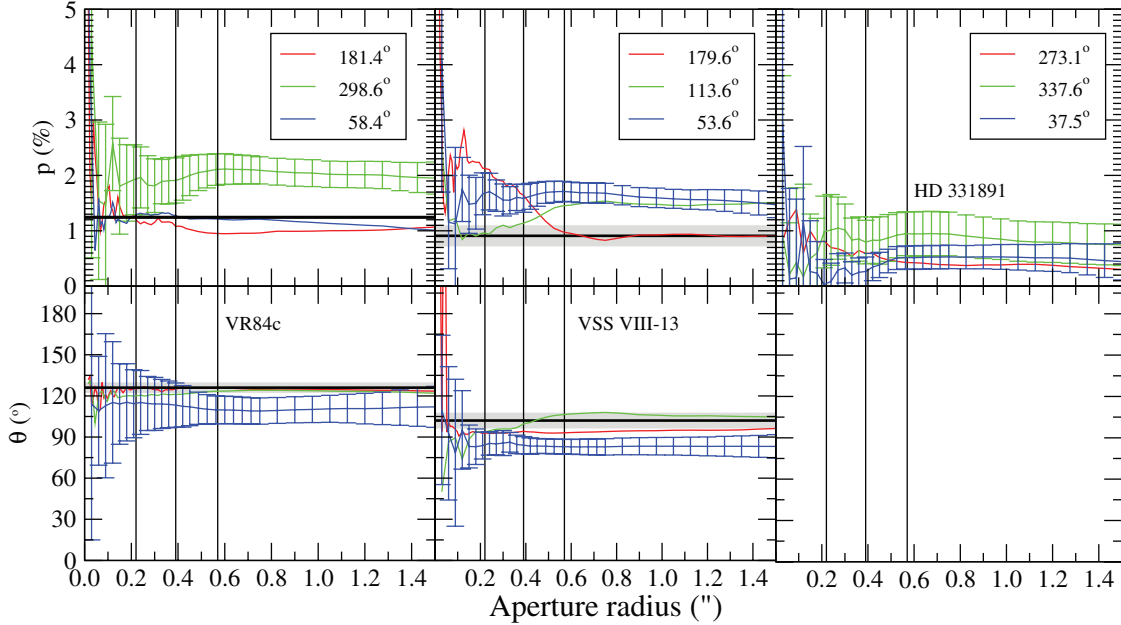


FIG. 6.—Results using the previous calibration. The thick solid lines show the ground-based results and the gray shaded areas show the uncertainties associated with those ground-based results. To avoid cluttering the plot, error bars are only shown for the cases where they do not overlap the ground-based results. The vertical solid lines mark the radii of the 1st, second, and third dark minima of the PSF. The values of θ are in the celestial reference frame (position angle east of north). The values of θ for HD 331891 bear no meaning and have therefore been excluded.

The unweighted average values of t_0 and t_{120} are 0.882 ± 0.008 and 0.837 ± 0.004 , respectively.

We apply these newly rederived coefficients to ascertain (p, θ) for our target stars with the results shown in Figure 7 (comparable directly to Fig. 6) and find the new calibration produces results consistent with the ground-based determinations in all cases. As an additional check we also apply the updated transmission coefficients to the data presented by B06 that suggested the original instrumental polarization. Figure 8 plots the

results from these reanalyzed data (it is similar to Fig. 2 from B06). As can be seen, reanalysis with the now improved determinations of the polarizer transmissivities produce (p, θ) results that are also now consistent with the ground-based data. The typical uncertainties associated with the profiles in Figure 8 are $\sigma_p \approx 1\%$ and $\sigma_\theta \approx 10^\circ$. The Cycle 11 data were not gathered using the additional dither points employed by this project; the polarimetric analysis performed on the archival data was improved through our updated calibration.

TABLE 4
THE NIC2 CALIBRATION FROM MULTIPLE ORIENTATIONS

Target	Polarizer	I_1	I_2	I_3	p (percent)	θ (deg)
[VR84] c	POL0L	22357.5	22855.3	22578.1	1.7 ± 0.3	115 ± 2
	POL120L	22914.5	22751.2	22721.1	0.8 ± 0.3	126 ± 6
	POL240L	22775.4	22650.3	23156.0	1.6 ± 0.5	122 ± 6
VSS VIII-13	POL0L	34362.8	34586.6	34804.0	1.1 ± 0.3	79 ± 10
	POL120L	34733.7	34816.8	34635.1	0.5 ± 0.2	85 ± 22
	POL240L	34969.2	34487.8	35190.2	1.3 ± 0.3	105 ± 6
HD 331891	POL0L	33817.0	33881.5	33636.2	0.6 ± 0.6	...
	POL120L	34154.7	34081.5	33929.6	0.7 ± 0.2	...
	POL240L	34244.6	34063.8	34054.5	0.4 ± 0.2	...

NOTE.—All results have been extracted from the apertures with a radius of 7.6 pixels ($0.58''$) and combine the data from the individual polarizers at the separate roll angles. I_1 , I_2 , and I_3 are in units of counts per second, averaged across the dithers, per polarizer, per orbit.

TABLE 5
THE NIC2 INSTRUMENTAL

Target	Polarizer	I_{nic}	Q_{nic}	U_{nic}	Q_{std}	U_{std}	p_{ins} (percent)	θ_{ins} (deg)
[VR84] c	POL0L	44574.1	-490.7	-573.8	-172.2	-529.9	0.7	94
	POL120L	44315.3	-112.7	-355.4	-171.2	-526.8	0.4	126
	POL240L	44294.8	-309.4	-613.7	-171.1	-526.6	0.4	106
VSS VIII-13	POL0L	68183.2	-680.6	281.6	-566.8	-252.4	0.8	141
	POL120L	67523.4	-325.9	52.6	-561.3	-249.9	0.6	116
	POL240L	67563.3	-787.7	-439.9	-561.7	-250.1	0.4	110
HD 331891	POL0L	66628.9	85.1	-399.8	0.0	0.0	0.6	...
	POL120L	66209.9	-315.8	297.2	0.0	0.0	0.7	...
	POL240L	66142.9	249.9	-121.8	0.0	0.0	0.4	...

NOTE.—The results from the NIC2 instrumental polarization tests. All results have been extracted from the apertures with a radius of 7.6 pixels.

5. DISCUSSIONS

We have used our data to perform a detailed investigation of the NIC2 instrumental polarization. This work was motivated, in part, by recent attempts to observe objects that have intrinsic polarizations of less than 5%. The previous calibrations were of sufficient accuracy to complete studies of more highly polarized targets but could not be used for high-accuracy polarimetry of targets with low intrinsic polarization. By obtaining high S/N observations of one unpolarized and two polarized standard stars, at three well-separated roll angles, we have been able to determine the level and orientation of the NIC2 instrumental polarization. By subtracting the instrumental polarization, in Stokes space, and improving upon the previous determination of the parallel transmission coefficients, we have successfully reproduced the polarimetric parameters of three standard stars

TABLE 6
ADJUSTING THE TRANSMISSION COEFFICIENTS

Target	PA (deg)	t_0	t_{120}	p (percent)	θ
[VR84] c	-178.6	0.8827	0.8346	1.2 ± 0.4	126 ± 3
	-61.4	0.8804	0.8369	1.3 ± 0.4	126 ± 5
	58.4	0.8883	0.8447	1.3 ± 0.4	127 ± 7
(B06)	-50.8	0.8914	0.8372	1.2 ± 0.1	125 ± 7
(B06)	-160.8	0.8897	0.8397	1.2 ± 0.1	124 ± 6
VSS VIII-13	179.6	0.8737	0.8335	0.9 ± 0.4	103 ± 12
	113.6	0.8771	0.8369	0.9 ± 0.4	103 ± 13
	53.6	0.8916	0.8425	0.8 ± 0.3	102 ± 8
HD 331891	-86.9	0.8804	0.8391	0.3 ± 0.4	...
	-22.4	0.8860	0.8302	0.5 ± 0.5	...
	37.5	0.8849	0.8391	0.4 ± 0.4	...
(B06)	-109.6	0.8629	0.8269	0.3 ± 0.1	...
(B06)	0.6	0.8718	0.8334	0.3 ± 0.1	...

NOTE.—Determining the parallel transmission coefficients that reproduce the ground-based results (taken from a 7.6 pixel aperture).

observed from the ground. These results were consistent for each standard observed at three different instrumental orientations in the celestial frame. Our results make this the most comprehensive polarimetric calibration of NIC2 to date (and quite likely the last) for direct imaging. We suggest this quantitative characterization of the NIC2 polarimetric system supersede the previous post-NCS-era polarimetric calibrations.

As the techniques used here require extremely precise photometry, there are many potential sources contributing to the uncertainties in determining p and θ . Highly precise photometric repeatability is limited by temporal, thermal, and metrological optical instabilities in the *HST* + NICMOS + instrumental system affecting the PSF, as well as spatial quantization and performance defects in the NIC2 detector and readout electronics. The measurement dispersions introduced by these (and perhaps other systematic) effects are carried through the SA99 analysis to determine $\sigma(p)$ and $\sigma(\theta)$. However, as we have been able to determine revised values for t_0 and t_{120} in 13 cases, we can assign uncertainties to these coefficients. By propagating these uncertainties through the polarimetric analysis we find that they dominate over the errors derived following SA99. For example, applying the new coefficients to [VR84] c, we find $p = 1.3\% \pm 0.4\%$, $\theta = 126^\circ \pm 5^\circ$ following SA99, but by propagating the uncertainties in t_k we find $p = 1.3\%(+0.7\%, -0.6\%)$, $\theta = 126^\circ(+10^\circ, -24^\circ)$.

The remaining uncertainties in the derived transmission coefficients do indeed dominate the statistical uncertainties from the photometry. What affect do these uncertainties have on the observationally determined values of p_{ins} and θ_{ins} ? Could these uncertainties be responsible for the observed instrumental polarization? As can be seen from Table 4, deviations between I_1 , I_2 , and I_3 , which that in an ideal detector would be invariant, are no greater than $\sim 2\%$, corresponding to a 1σ error in p_{ins} of only 0.1%. However, a more accurate way to determine p_{ins} requires observations of an unpolarized standard star across

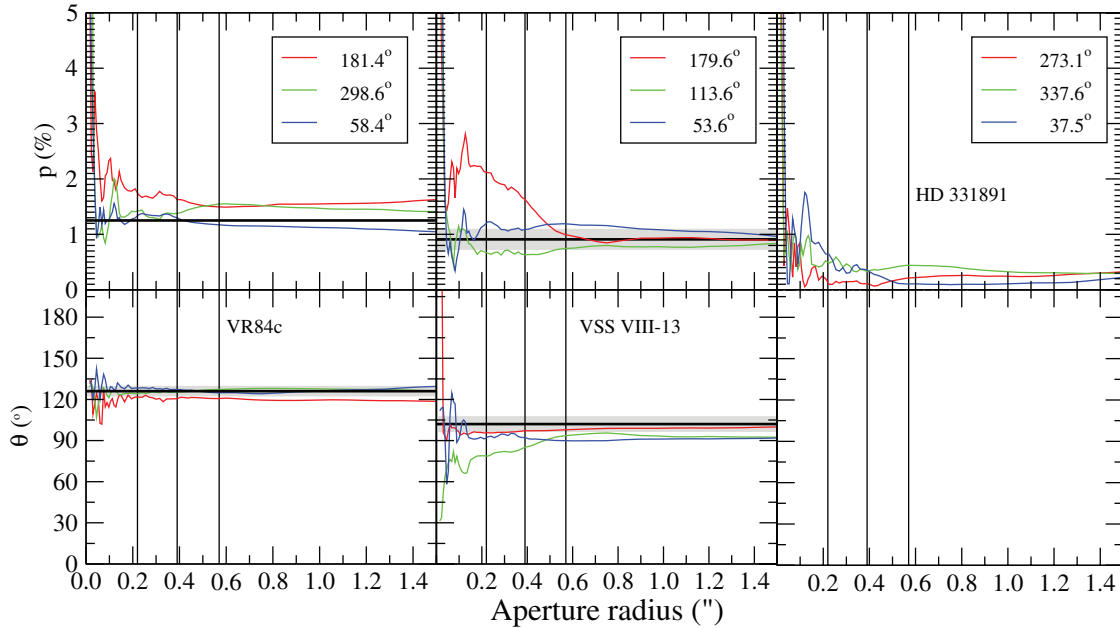


FIG. 7.—Results using the new calibration. The same convention is used as for Fig. 6. All results are now consistent with the ground-based data. The values of θ for HD 331891 bear no meaning and have therefore been excluded.

the whole detector area to map any field dependence in the polarization. Because our results have been derived from dithered observations, any field dependence that might exist in the polarization could mimic an instrumental polarization on our data. Such a study cannot be done with the current data, so it is not possible to assert p_{ins} at such a level. Instead, it is

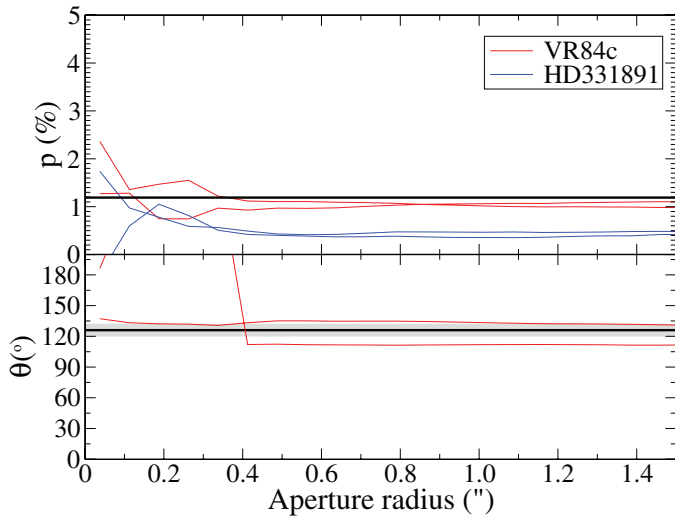


FIG. 8.—Checking the new calibration against the data that originally suggested an instrumental polarization. The errors bring all consistent with the ground-based results. The values of θ for HD 331891 have been omitted for clarity and because they bear no meaning.

more appropriate to present the 0.6% value as an instrumental upper limit; p_{ins} could indeed be zero.

What then happens to the rest of our analysis if p_{ins} is indeed zero? To test this, we have rederived the values of t_k without subtracting p_{ins} in the (Q, U) plane. Taking this approach we find $t_0 = 0.884 \pm 0.008$ and $t_{120} = 0.838 \pm 0.003$, which is entirely consistent with the results taken from the instrumentally subtracted Q, U . So, again we find that the errors in t_k dominate the uncertainties in the measured values of p and θ . As these uncertainties have been derived from 13 separate observations that are all subjected to the photometric uncertainties themselves, we are left with the understanding that this calibration is limited by the photometric repeatability of individual observations. This includes all of the known affects presented in § 2.

When comparing the new parallel transmission coefficients with the old it can be seen that t_{120} is consistent with both calibrations; only t_0 has needed to be changed, albeit only by $\sim 0.5\%$. Applying this correction to previous studies of *highly* polarized targets will therefore not alter the results by any significant amounts. However, when applied to targets with low polarization this tweak has a tremendous affect.

5.1. Recommended Observing Strategy

In the cases where the target is spatially resolved and does not contain a strong point source, observers should bin their data to 3×3 pixels (in order to meet the diffraction limit of the instrument). Dithering can be used in the usual way to increase

TABLE 7
THE NEW POLARIMETRIC COEFFICIENTS

Polarizer	ϕ_k (deg)	η_k	l_k	t_k
POL0L	8.84	0.7313	0.1552	0.882 ± 0.008
POL120L	131.42	0.6288	0.2279	0.837 ± 0.004
POL240L	248.18	0.8738	0.0673	0.9667

NOTE.—The new NIC2 polarization coefficients as derived by this program.

spatial resolution as well as to mitigate bad pixel affects. However, the signal-to-noise ratio will still limit the accuracy of p and θ determinations, especially in targets whose surface brightnesses vary significantly on small spatial scales, i.e., comparable to, or smaller than, the diffraction limit.

The case of a spatially unresolved source is not so straightforward. As explained above, the uncertainties in t_k do dominate the accuracy of p and θ . However, as this study has shown, nonrepeatabilities in aperture photometry (in the absence of well-dithered observations) suggest that unidentified outliers can readily bias polarimetric analysis independent of the intrinsic accuracy of the polarimetric calibration. The data have been carefully inspected to identify photometrically deficient pixels by comparing each individual profile to the dispersion in the photometry measured from ~ 12 pointings. This study has shown that $\sim 10\%$ of all target pointings (even those avoiding known photometrically deficient areas of the detector like the coronagraphic hole) will include uncorrectable bad pixels that affect the measured polarization. A method to robustly detect, and reject, photometric measures degraded by such effects is to perform a target raster with a dither pattern with three or more pointings. The step size should be more than 3 times greater than the FWHM of the PSF to avoid persistence. Encircled energy (intensity) profiles should be derived independently from each observation (dither point). With a sufficiently large number of dither points, a sigma clip can then be used to determine whether an individual profile is deviant or not. The greater number of dithers used, the more accurate this clip will be. For small numbers of dither points (not optimally recommended) medianing can be used to coarsely reject outliers. The average of the remaining profiles can then be used to derive p and θ from the coefficients presented in Table 7.

This study has shown that the affects of the IPRFs are largely mitigated by effective dithering. However, the uncertainty in the calibration of t_k ultimately dominates the accuracy of (p, θ) polarimetric analysis for sources with intrinsically low polarization, if observed with a sufficient number of optimally placed dither positions; observers need not be concerned by the IPRF. Since observations through the three polarizers are not simultaneously obtained, temporal instabilities in the *HST* + NICMOS PSF are still a concern and the effects are readily seen in Figures 2, 5, 6, and 7. Outside an aperture of radius $0.58''$,

the PSF affects are seen to be alleviated. Inside this radius, the errors in p and θ rise rapidly, and it will be left to the discretion of the observer to weigh their required accuracy to the possible results of beam depolarization.

6. CONCLUSIONS

In a nonideal imaging polarimeter, such as NICMOS, it is essential to observe several polarimetric standards, at three well-separated position angles through each polarizer, in order to fully characterize the instrumental polarization. The additional roll angles remove the uncertainties in the (unknown) parallel transmission coefficients and allow rotation of any instrumental polarization with respects to the equatorial frame. Using this technique we have placed an upper limit to the NIC2 instrumental polarization of 0.6%. With a known value for the Stokes I parameter, the instrumental polarization can be transformed into the Q, U plane and be subtracted. New parallel transmission coefficients can then be determined numerically by comparing p and θ with that of the a priori well-determined calibration standards. Following this approach we have determined the t_0 and t_{120} coefficients to be 0.883 ± 0.004 and 0.837 ± 0.004 , respectively. As with the previous calibrations of the NIC2 polarimeter, we held t_{240} constant at 0.9667. The t_{120} coefficient is consistent with the previous calibration, but our knowledge of t_0 has been improved, resulting in a change in its previously determined value by $\sim 0.5\%$. Such a small change in t_0 does not warrant the reanalysis of previous NIC2 imaging polarimetry data of *highly* polarized ($p > 5\%$) targets but is significant for targets with intrinsically low polarization fractions.

As we use 13 determinations of t_k , we are able to assign 1 σ uncertainties to the calibration coefficients. Propagating these uncertainties through the polarimetric analysis, we find that they dominate all other sources of error. Applying these adjusted values of t_k to this (and the archived) calibration data, we find that NIC2 is now capable of confidently detecting polarizations at a level of $\approx 1.0\%$. The uncertainties associated with such measurements are $\pm 0.6\%$ and $\pm 15^\circ$ in p and θ , for sources at the $\approx 1\%$ level of intrinsic polarization. This is the first time that such a level of accuracy has been achieved with the NICMOS polarization calibration. This improved calibration opens a new domain for observational investigations with *HST* by enabling very high-precision polarimetry of intrinsically very low polarization sources.

We are grateful to the referee for a thorough reading of this manuscript. Support for Proposal number HST-GO-10839.01-A was provided by NASA through a grant from the Space Telescope Science Institute, which is operated by the Association of Universities for Research in Astronomy, Incorporated, under NASA contract NAS5-26555.

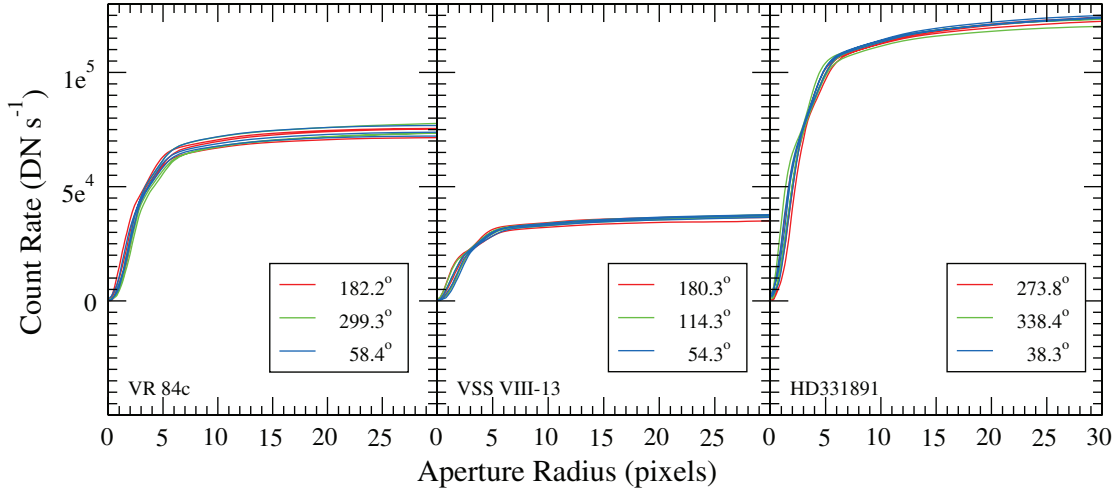


FIG. 9.—NIC1 radial profiles. For each target, the encircled count rate for each polarizer and celestial orientation is shown.

APPENDIX

THE NIC1 CALIBRATION

For the NIC1 observations, the individual pointings for each polarizer were not dithered around the 12-point pattern used for the NIC2 observations. However, the observations from each separate polarizer were dithered so as to avoid persistence. The pointings were also placed on an area of NIC1 where the quantum efficiency (QE) gradients are particularly shallow and where the QE is reasonably high. This area was also sufficiently far from any “grotty” pixels and sufficiently far from the edge of the detector.

As there are only single pointings per polarizer, the data analysis for the NIC1 data is less complicated than for the NIC2 case. The extracted radial profiles from each polarizer (and pointing) at each roll angle are shown in Figure 9. For these

profiles we can only define the S/N using the photon noise. As there are only single pointings in each NIC1 polarizer, it is impossible to perform the iterative 2σ clipping technique employed for NIC2. Therefore all NIC1 profiles must be included in the analysis. Although there is no statistical way to tell if the profiles in Figure 9 are robust, we can at least see that all profiles are consistent with each other. This is likely due to the care taken in avoiding uncorrectable bad pixels.

At the radius of the third NIC1 dark Airy minimum (given by an aperture with $r = 7.0$ pixels, assuming a central wavelength of $1.05\ \mu\text{m}$ and a 2.281 m aperture) the respective signal-to-noise ratios for [VR84] c, VSS VIII-13, and HD 331891 are 257, 180, and 330 when averaged across the three polarizers.

TABLE 8
THE NIC1 CALIBRATION FROM MULTIPLE ORIENTATIONS

Target	Polarizer	I_1	I_2	I_3	p (percent)	θ (deg)
[VR84] c	POL0S	64292.5	68734.3	65147.3	4.1 ± 0.1	116.5 ± 0.5
	POL120S	67785.9	64160.6	66039.8	6.47 ± 0.06	131.6 ± 0.6
	POL240S	66771.2	64206.3	68756.5	5.1 ± 0.2	122.8 ± 0.2
VSS VIII-13	POL0S	31156.2	32770.7	32472.4	3.1 ± 0.2	91 ± 1
	POL120S	32393.0	32412.3	31762.6	3.0 ± 0.1	83 ± 2
	POL240S	33123.9	31812.0	32638.4	2.9 ± 0.2	94 ± 2
HD 331891	POL0S	107931	107057	109394	1.3 ± 0.1	...
	POL120S	108864	109376	108867	0.63 ± 0.04	...
	POL240S	108221	108756	109656	1.06 ± 0.06	...

NOTE.—All results have been extracted from the apertures with a radius of 7.0 pixels and combine the data from the individual polarizers at the separate roll angles.

TABLE 9
THE NEW NIC1 POLARIMETRIC COEFFICIENTS.

Polarizer	ϕ_k (deg)	η_k	l_k	t_k
POL0S	1.42	0.9717	0.0144	0.7760
POL120S	116.30	0.4771	0.3540	0.57 ± 0.01
POL240S	258.72	0.7682	0.1311	0.69 ± 0.01

NOTE.—The new polarization coefficients, as derived by this program, for NIC1 polarimetry.

The theoretical NIC1 achievable accuracies are approximately 1.5% with an uncertainty of $\pm 0.2\%$ and $1.0\% \pm 0.3\%$.

At 1.21 μm , Whittet et al. (1992) give [VR84] c a polarization of $3.19\% \pm 0.05\%$ at $118^\circ \pm 1^\circ$ and VSS VIII-13 a polarization of $2.21\% \pm 0.3\%$ at $96^\circ \pm 1^\circ$. As there is no data for HD 331891 at this wavelength, we assume that this target is unpolarized. The polarizations and uncertainties are carried through the Serkowski correction and are presented in Table 2.

Except for the 2σ clipping, the NIC1 data was treated exactly like the NIC2 data. The calibration data from the multiple orientations are presented in Table 8. The NIC1 instrumental polarization was then determined to be $1.3\% \pm 0.9\%$ at an orientation of $151^\circ \pm 18^\circ$. This instrumental polarization was subtracted in (Q, U) space, and the parallel transmission coeffi-

cients were rederived on an orbit by orbit basis. The coefficients and uncertainties that bring all the data consistent with the ground-based data are $t_{120} = 0.57 \pm 0.01$ and $t_{240} = 0.69 \pm 0.01$. All the coefficients to be used in NIC1 polarimetric observations are shown in Table 9. Applying these new calibration coefficients to the original data brings all polarimetric standards consistent with the ground-based results.

Compared with the previous NIC1 calibration coefficients ($t_{120} = 0.5934$ and $t_{240} = 0.7173$), the coefficients derived here are lower. In the previous instance the coefficients were derived from observations of an unpolarized standard, and not from data at three well-separated roll angles. However, the data used in this calibration have not been dithered over the detector (as in the case of the NIC2 data); instrumental affects will still be present. The fact that the uncertainties in the newly derived coefficients for NIC1 are larger than for the NIC2 case reflects this finding. Propagating the coefficient uncertainties through the polarimetric analysis results in polarization measures of $5\%(+6\%, -2\%)$ at $123^\circ(+24^\circ, -12^\circ)$ for [VR84] c, $3\%(+6\%, -2\%)$ at $94^\circ(+85^\circ, -27^\circ)$ for VSS VIII-13 and $3\%(+5\%, -3\%)$ for HD 331891. We therefore recommend that NIC1 only be considered for observations of targets that are postulated to have an intrinsic polarization of greater than 4% per resolution element. The uncertainties in polarization measures from such a target will, however, be large.

REFERENCES

- Antonucci, R. R. J., & Miller, J. S. 1985, *ApJ*, 297, 621
- Barker, E., et al. 2007, NICMOS Instrument Handbook Version 10.0, http://www.stsci.edu/hst/nicmos/documents/handbooks/current_NEW/nicmos_ihb.pdf
- Batcheldor, D., Robinson, A., Axon, D., Hines, D. C., Sparks, W., & Tadhunter, C. 2006, *PASP*, 118, 642
- Capetti, A., Axon, D. J., Chiaberge, M., Sparks, W. B., Duccio Macchetto, F., Cracraft, M., & Celotti, A. 2007, *A&A*, 471, 137
- Capetti, A., Macchetto, F., Axon, D. J., Sparks, W. B., & Boksenberg, A. 1995, *ApJ*, 452, L87
- Capetti, A., et al. 2000, *ApJ*, 544, 269
- Feretti, L., Giovannini, G., Klein, U., Mack, K.-H., Sijbring, L. G., & Zech, G. 1998, *A&A*, 331, 475
- Hines, D. C. 2002, in Proc. 2002 HST Calibration Workshop, 2002 October, Hubble after the Installation of the ACS and the NICMOS Cooling System, ed. S. Arribas, A. Koekemoer, & B. Whitmore (Baltimore: STScI), 258
- Hines, D. C., Schmidt, G. D., & Schneider, G. 2000, *PASP*, 112, 983
- Kuhn, J. R., Potter, D., & Parise, B. 2001, *ApJ*, 553, L189
- Meakin, C. A., Hines, D. C., & Thompson, R. I. 2005, *ApJ*, 634, 1146
- Schmidt, G. D., Hines, D. C., & Swift, S. 2002, *ApJ*, 576, 429
- Schneider, G. 2004, *Adv. Space Res.*, 34, 543
- Schneider, G., & HST/GO 10177 Team 2005, in *BAAS*, Vol. 37, 1168
- Serkowski, K. 1973, in *IAU Symp. 52, Interstellar Dust and Related Topics*, ed. J. M. Greenberg, & H. C. van de Hulst (Dordrecht: Reidel Publishing Company), 145
- Serkowski, K., Mathewson, D. L., & Ford, V. L. 1975, *ApJ*, 196, 261
- Silber, J., Gledhill, T., Duchêne, G., & Ménard, F. 2000, *ApJ*, 536, L89
- Simpson, J. P., Colgan, S. W. J., Erickson, E. F., Burton, M. G., & Schultz, A. S. B. 2006, *ApJ*, 642, 339
- Simpson, J. P., Colgan, S. W. J., Erickson, E. F., Hines, D. C., Schultz, A. S. B., & Trammell, S. R. 2002, *ApJ*, 574, 95
- Smith, J. E., Robinson, A., Alexander, D. M., Young, S., Axon, D. J., & Corbett, E. A. 2004, *MNRAS*, 350, 140
- Sparks, W. B., & Axon, D. J. 1999, *PASP*, 111, 1298
- Su, K. Y. L., Hrivnak, B. J., Kwok, S., & Sahai, R. 2003, *AJ*, 126, 848
- Tadhunter, C. N., et al. 2000, *MNRAS*, 313, L52
- Thompson, R. I., Rieke, M., Schneider, G., Hines, D. C., & Corbin, M. R. 1998, *ApJ*, 492, L95
- Turnshek, D. A., Bohlin, R. C., Williamson, R. L. II, Lupie, O. L., Koornneef, J., & Morgan, D. H. 1990, *AJ*, 99, 1243
- Ueta, T., Murakawa, K., & Meixner, M. 2005, *AJ*, 129, 1625
- Vernet, J., Fosbury, R. A. E., Villar-Martín, M., Cohen, M. H., Cimatti, A., di Serego Alighieri, S., & Goodrich, R. W. 2001, *A&A*, 366, 7
- Whittet, D. C. B., Martin, P. G., Hough, J. H., Rouse, M. F., Bailey, J. A., & Axon, D. J. 1992, *ApJ*, 386, 562
- Wielebinski, R. 1995, *Rev. Mod. Astron.*, 8, 185–200
- Wilking, B. A., Lebofsky, M. J., & Rieke, G. H. 1982, *AJ*, 87, 695